Original research article

Numerical study of mass and heat transport within a ceramic porous tank

Ramzi Rzig[1,2,*], Minyar Mnakri[3], Nidhal Ben Khedher[2,4]

[1] *Become: Technology, Science, AI & Automation Lab, 63 Street of Tolbiac, 75013 Paris, France*

[2] *Thermal and Energy Systems Studies Laboratory, National School of Engineers of Monastir, University of Monastir, Monastir 5019, Tunisia*

[3] *Laboratory of Spectroscopic Characterization and Optical Materials LaSCOM, Sfax University, Sfax 3029, Tunisia*

[4] *Department of Mechanical Engineering, College of Engineering, Hail University, Hail 55476, Saudi Arabia*

* Corresponding author: Ramzi Rzig, rzigramzi10@gmail.com

Abstract: In porous media, the thermal transfer phenomenon is widely applied in diverse energy-intensive industrial processes. This research paper aims to elucidate the simultaneous transfer of mass and heat within a ceramic porous tank. To simulate these transport phenomena, a numerical method is developed: Control Volume Finite Element Method (CVFEM), in conjunction with the utilization of a free mesh generator called Gmsh. The study showcases numerous simulation results that depict the transport phenomenon, such as the three-dimensional evolution of three parameters (temperature, saturation and pressure) during the heating of the ceramic tank. By employing this numerical model, a more comprehensive comprehension of these transport phenomena can be achieved.

Keywords: porous media; ceramic porous tank; CVFEM; Gmsh; transport phenomenon

1. Introduction

In porous media, mass and heat transport constitutes a foundational subject in the realms of engineering and physics. Porous media denotes substances with interconnected empty spaces that permit the flow of fluids such as air, water, or gases. Various examples of porous media encompass soils, rocks, biological tissues, as well as numerous other natural and synthetic materials. Heat transfer in porous media entails the conveyance of thermal energy through the material as a result of temperature discrepancies between the two phases: fluid and solid. This transpires via mechanisms like conduction, convection, and radiation. Conversely, mass transfer revolves around the movement of fluid or gas molecules through the porous material, predominantly propelled by concentration gradients. The study of porous media, in particular the mass and heat transfer, bears significance across an extensive array of applications, including geothermal energy systems, filtration procedures, catalytic reactors, and many more. Grasping the intricate behavior of these systems necessitates the amalgamation of experimental, analytical, and numerical techniques.

Building upon the theoretical frameworks presented by Luikov[1] and Whitaker[2], a mathematical framework for modeling transport phenomena in porous media has been devised. This framework incorporates dynamic variables such as temperature, pressure, and saturation. To obtain numerical solutions, the researchers chose the Control Volume Finite Element Method (CVFEM), as it has demonstrated exceptional suitability for efficiently and swiftly implementing the linearization technique. Additionally, the difference finite solution is

overused in the study of several problems in porous media[3,4]. Also, the CVFEM has been widely involved[5], further enhancing the methodology available for analyzing these systems. Recently, a numerical model was created to visualize the movement of immiscible fluids through a porous medium in vertical annular microtubes using electroosmotic flow[6].

Currently, sand tanks or sand batteries have gained significant global attention due to their impressive thermal capabilities for heat storage within sand particles. Sand batteries represent a specific type of battery that incorporates sand as a crucial component within the anode. The concept behind sand batteries stems from the notion that the abundant and cost-effective resource of sand can be utilized to develop a battery technology that is both sustainable and environmentally friendly. The fundamental principle underlying sand batteries is that the individual sand particles function as electrode materials, wherein the extensive surface area of the sand grains facilitates substantial electrochemical reactions. To enhance its electrical conductivity, the sand is typically coated with a thin layer of conductive material, such as carbon.

There is a considerable amount of literature available on the use of sand tanks for studying sediment transport: a study on the effects of sand grains on transport in a sand reservoir is established[7]. For solar concentrators, the thermal performance of a sand-basalt heat storage system has been studied[8]. Recently, Cao et al.[9] have numerically analyzed a PCM reservoir by applying natural water convection. Also, an experimental study of the dynamics of fresh-salt water in sand reservoirs has been developed[10]. In 2022, Thien et al. have studied the effects of reservoir color with sand and shelter[11]. Moreover, for the foundation of the reservoir with the hot sand, an experimental analysis of the characteristics (solidification and migration) of the solar salt is applied[12]. The reservoir (liquid storage) earthquakes on flexible soil are given by the study of Lee et al.[13]. More recently, a seismic loading analysis in steel tank buckling is established[14]. A 3D numerical analysis of the flow in a thermal energy reservoir is studied[15].

Sand batteries are currently in the initial phases of development, and there exist numerous obstacles that must be addressed before achieving commercial viability.

The aim of this paper is to investigate the thermal transfer phenomenon during heating a ceramic-based tank. The research presents three-dimensional analyses of temperature, saturation, and pressure variations within the ceramic tank. Several numerical results demonstrate the originality of our code in examining the coupled mass and heat transfer occurring inside the tank: temperature (T), saturation (S), pressure (P).

2. Numerical model

A numerical simulation is presented in the present model to study the thermal transfer process within a ceramic porous tank. The tank's geometry is depicted in **Figure 1**.
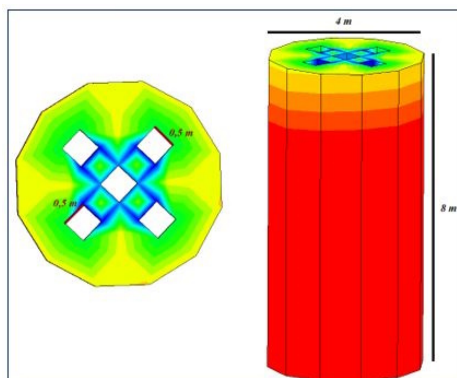
Figure 1. Dimensions of tank.

Our tank has a cylindrical shape (Length 8 m & Width 4 m) with 5 square tubes with sides of 0.5 m. These tubes heat the grains of sand to a high temperature.

2.1. Equations system

The equations system is defined by Whitaker[2]. The assumptions for the establishment of a numerical system of mass and heat transfer in porous media are:

● We consider our environment as a homogeneous and isotropic environment. The three phases: solid, liquid and gas are thermodynamically in equilibrium.

● We negligee radiative heat transfer: viscous dissipation and compression-work.

● The diffusion is established as dispersion and tortuosity and the phase of gas is considered as ideal phase.

In porous media, macroscopic equations of heat and mass transport are presented.

2.2. Generalized Darcy's Law

The law of Darcy provides the following average velocities:

● Phase of liquid:

$$\overline{V}_l = -\frac{KK_l}{\mu_l}\left[\nabla\left(\overline{P}_g{}^g - P_c\right) - \overline{\rho}_l{}^l g\right] \tag{1}$$

with $P_c = \overline{P}_g{}^g - \overline{P}_l{}^l$ presents the capillary used pressure.

● Phase of gas:

$$\overline{V}_g = -\frac{KK_g}{\mu_g}\nabla\overline{P}_g{}^g \tag{2}$$

2.3. Conservation of mass

● Phase of liquid:

For the phase of liquid, given that the liquid density is constant, the mass conservation equation is:

$$\frac{d\varepsilon_l}{dt} + \nabla(\overline{V}_l) = -\frac{\dot{m}}{\overline{\rho}_l} \tag{3}$$

and $\dot{m}$ presents the rate of evaporation mass.

Liquid's fraction volume is: ε_l.

● Phase of gas:

The mass conservation's equation is:

$$\frac{d\overline{\rho_g}}{dt} + \nabla\left(\overline{\rho_g}{}^g\overline{V}_g\right) = \dot{m}_g \tag{4}$$

and $\overline{\rho_g}{}^g$ presents the average intrinsic density of gas, which is treated as an ideal mixture of perfect gases.

● Phase of vapor:

$$\frac{d\overline{\rho_v}}{dt} + \nabla\left(\overline{\rho_v}{}^g\overline{V}_v\right) = \dot{m}_v \tag{5}$$

$$\overline{\rho_v}{}^g\overline{V}_v = \overline{\rho_v}{}^g\overline{V}_g - \overline{\rho_g}{}^g D_{eff}\nabla\left(\frac{\overline{\rho_v}}{\overline{\rho_g}{}^g}\right) \tag{6}$$

and D_{eff} presents the diffusion effectiveness coefficient of vapor phase. Also, this coefficient considers the resistance to diffusion caused by the tortuosity and constriction terms.

2.4. Conservation of energy

The equation of energy conservation is:

$$\frac{\partial}{\partial t}(\overline{\rho C_P}\bar{T}) + div\left[\left(\bar{\rho}_l{}^l C_{Pl}\overline{V_l} + \sum_{k=a,V}\overline{\rho_k}{}^g C_{Pk}\overline{V_k}\right)\bar{T}\right] = \nabla\left(\lambda_{eff}.\nabla\bar{T}\right) - \Delta H_{vap}\,\dot{m}_v \tag{7}$$

at temperature T (Kelvin), ΔH_{vap} is the heat latent of vaporization,

and λ_{eff} notes the effective thermal conductivity of the medium,

also $\overline{\rho C_p}$ presents the capacity heat of the medium defined as bellow:

$$\overline{\rho C_p} = \bar{\rho}_s C_{ps} + \bar{\rho}_l C_{pl} + \bar{\rho}_a C_{pa} + \bar{\rho}_v C_{pv} \tag{8}$$

which $\bar{\rho}_s C_{ps}$, $\bar{\rho}_l C_{pl}$, $\bar{\rho}_v C_{pv}$ and $\bar{\rho}_a C_{pa}$ presents the heat capacities of mass of three phases (liquid, gas, solid).

2.5. Relations of thermodynamic

In our model, we have used the following pressure of vapor phase:

$$P_v = P_{veq}(T, S)$$

with S presents the saturation of liquid explained as bellow:

$$S = \frac{\varepsilon_l}{\varepsilon} \tag{9}$$

The pressure (gas) is defined by:

$$\bar{P}_i = \frac{\bar{\rho}_i}{M_i}R\bar{T}\;; i = a, v \tag{10}$$

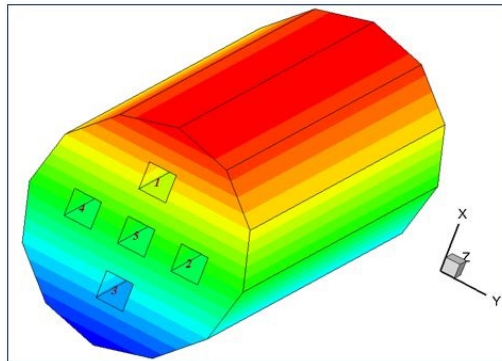$$\bar{P}_g = \bar{P}_a + \bar{P}_v\,, \bar{\rho}_g = \bar{\rho}_a + \bar{\rho}_v$$

For the vapor phase, the pressure is:

$$\frac{P_v}{P_{vs}} = \exp(-\frac{2\sigma M_v}{r\rho_l RT}) \tag{11}$$

3. Conditions of model

For our equations system, the conditions are defined as shown below (refer to **Figure 2**):

● Hot air enters through the tubes (T = 100 °C; V = 10 m/s; CV_{amb} = 0.001).

● The grains of the ceramic are heated step by step: let's start with the grains closest to the cavities towards the furthest grains.

Figure 2. Model's conditions.

Conditions of our model:

Exchanging cavities:

$$\left[\lambda_{eff}\frac{d\langle T\rangle}{dX_i}+\Delta H_{vap}\rho_l\langle V_l\rangle n_i\right]=h_t(\langle T\rangle-T_\infty)\tag{12}$$

For evacuation and evaporation terms, we use the following flow of mass:

$$[\rho_l\langle V_l\rangle+\langle\rho_v\rangle^g\langle V_v\rangle]n_i=h_m(C_{vs}-C_{v\infty})\tag{13}$$

On exchanging faces, the pressure is considered as an atmospheric one:

$$[\langle P_g\rangle^g]=P_{atm}\tag{14}$$

In bottom, the face is treated as impermeable and adiabatic.

$$\left[\lambda_{eff}\frac{d\langle T\rangle}{dX_i}+\Delta H_{vap}\rho_l\langle V_l\rangle n_i\right]=0\tag{15}$$

$$[\rho_l\langle V_l\rangle+\langle\rho_v\rangle^g\langle V_v\rangle]n_i=0\tag{16}$$

$$\left[\frac{d\langle P_g\rangle^g}{dX_i}\right]=0\tag{17}$$

The transport coefficients within the cavities of the tank are elucidated in the following **Table 1**:

Table 1. Thermal transfer coefficients within tank cavities[16].

Coefficients	Cavities
h_{ht}	$\dfrac{\lambda\times0.023\times Re^{4/5}\times Pr^{1/3}}{D}$
h_{mt}	$\dfrac{0.023\times D_{C,D}\times Sc^{1/3}\times Re^{4/5}}{D}$
Validity conditions	$10^4<Re<1.2\times10^5$ $0.6\le Pr\le160$ $0.6\le Sc\le160$
Variables	$Re=\dfrac{\rho_a v_a D}{\mu_a}$ $Pr=\dfrac{C_a\mu_a}{\lambda_a}$ $Sc=\dfrac{\vartheta_a}{D_{A,B}}$

with:

h_{ht}: coefficient of heat transfer $\frac{\text{w}}{\text{m}^2{}^\circ\text{C}}$,

h_{mt}: coefficient of mass transfer $\frac{\text{m}}{\text{s}}$,

$D_{C,D}$: presents the term of diffusion (vapor in air) defined as bellow:

$$D_{C,D}=D_{\text{vap,air}}=0.26\times10^{-4}\ \frac{\text{m}^2}{\text{s}}$$

$L=8$ m: ceramic tank length.

4. Numerical solution

Our system of equations is established based on numerical CVFEM method, as described in the studies[17,18]. The elements triangular are used for the construction of volume control: providing flexibility in grid design. Additionally, this numerical method guarantees the preservation of flux. To generate the mesh required for the simulation, we employ the free mesh generator Gmsh[19] (**Figure 3**).

Figure 3. Free mesh Gmsh.

The code is written by FORTRAN and enables us to simulate the movement of mass and heat within the tank. Based on this presented model, we aim to gain a comprehensive analysis of the thermal behavior and mass transport phenomena occurring within the ceramic tank. This recent research provides several information into the thermal transfer mechanisms, contributing to the advancement of ceramic tank design and optimization in various practical applications.

The objective of our code is to plot the evolutions of the three parameters (T; S; P) as a function of time and to have a 3D visualization of these parameters.

5. Results and discussions

In this part, we showcase the outcomes derived from our code implementation, specifically focused on investigating the mass and heat transport occurring within the ceramic tank. Our numerical study encompasses the analysis of temperature, saturation, pressure, and water content variations. To simulate the three-dimensional transfer term that transpire inside the tank, we employ the Gmsh free mesh generator, as illustrated in the following **Figure 4**:
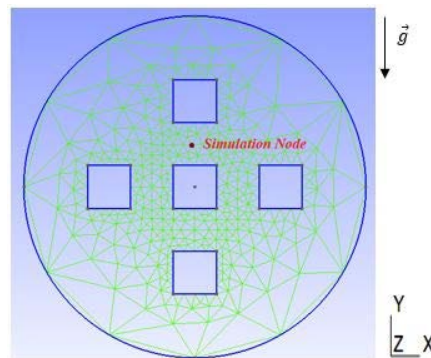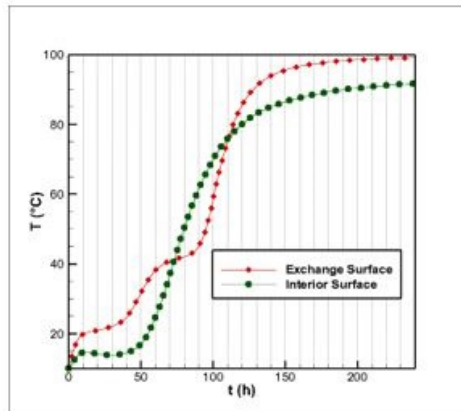

Figure 4. Tank meshing.

Numerical parameters used in this code are presented in the following table (**Table 2**):

Table 2. Parameters of model.

T (°C)	S (%)	V (m/s)	Po (%)	CV_{amb}	P_{amb} (atm)
100	50	10	30	0.001	1

5.1. Temperature evolution

In **Figure 5**, we show the evolution of temperature for two modes: exchange surface and interior surface (**Figure 5**).
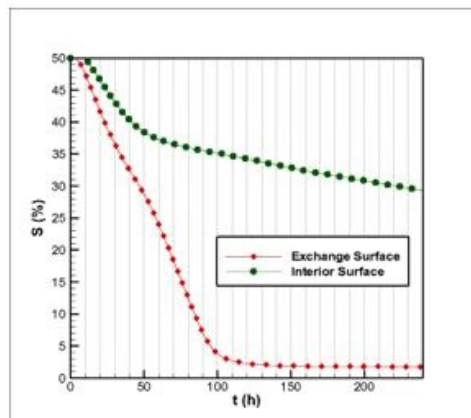

Figure 5. Temperature evolution.

Referring to **Figure 5**, we can observe that the profile of temperature is rapid for node closest to the exchange surface which promotes the heat exchange during the drying process.

5.2. Saturation evolution

In this part, we present the evolution of saturation in liquid (**Figure 6**).

Figure 6. Saturation evolution.

A comparison of the liquid saturation evolution is depicted in **Figure 6**. The figure illustrates a gradual reduction over time, with the rate of decrease being relatively slower for the nodes located in the middle and at the bottom of the tank.

5.3. Pressure evolution

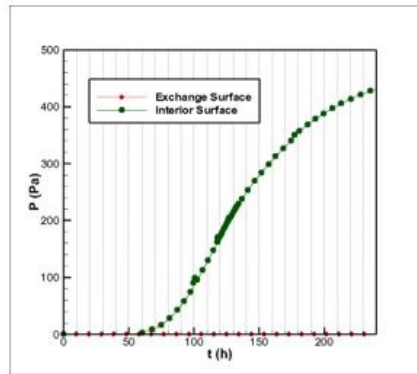For this part, we depict the pressure evolution (**Figure 7**).

Figure 7. Pressure evolution.

From the information presented in **Figure 7**, it can be deduced that the significant pressure peak is associated with the node located within the tank containing a substantial quantity of water.

5.4. Water content evolution

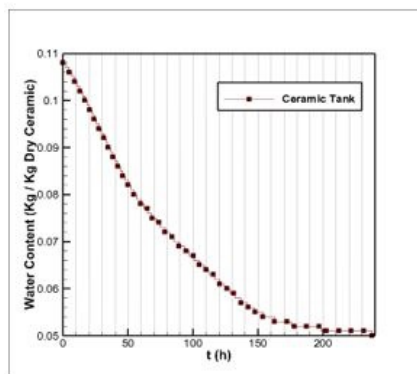Also, we have studied the evolution of water content as shown in **Figure 8**.

Figure 8. Water content evolution.

The observation from **Figure 8** reveals a gradual decrease in water content over time, eventually approaching zero.

To better understand the mechanisms that arise during thermal transport within the tank, we have shown:

- Spatial and temporal variations of three parameters (T; S; P) (**Figures 9–11**).
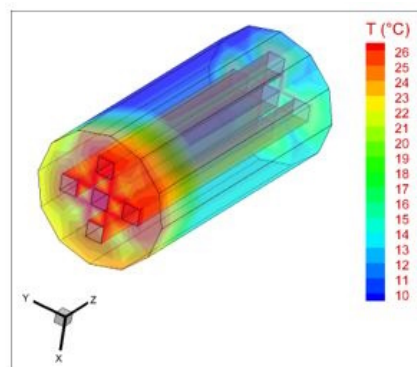- Slice's view (**Figures 12–14**).

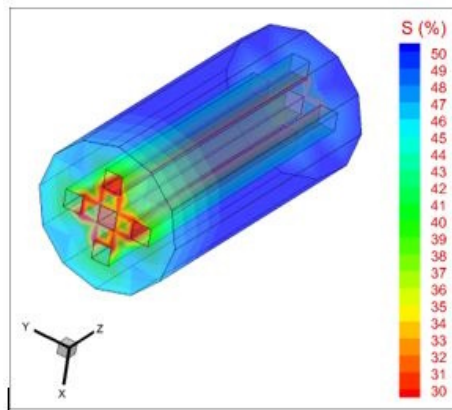**Figure 9.** Temperature 3D breakdown.
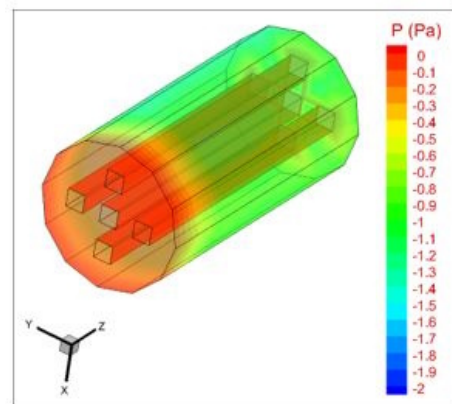
Figure 10. Saturation 3D breakdown.

Figure 11. Pressure 3D breakdown.

Referring to findings presented in **Figures 9–11**, several observations can be made:

● Heat and mass exchange exhibit higher intensity in the cavities compared to the interior of the tank. This disparity can be attributed to the existence of temperature slope that facilitates the energy provision required for the evaporation process.

● The cavities promote more rapid and intense liquid evaporation, leading to accelerated changes over time.

● Conversely, the interior of the tank experiences slower heat and mass transfer dynamics.
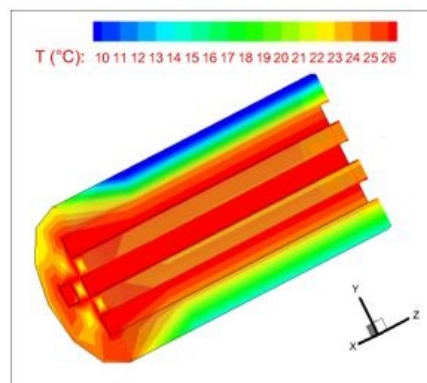

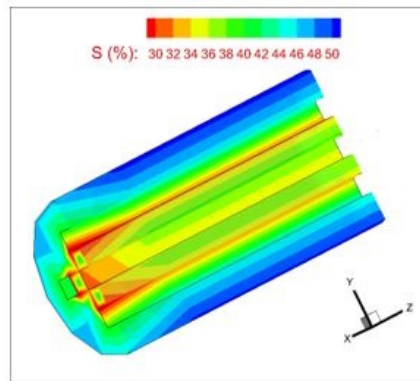**Figure 12.** Slice's view for temperature evolution.

9

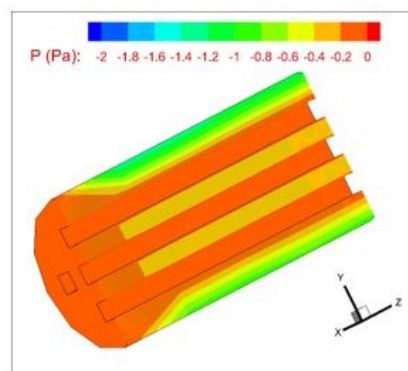**Figure 13.** Slice's view for saturation evolution.

Figure 14. Slice's view for pressure evolution.

By examining **Figures 12–14**, it becomes apparent that the exchange cavities exhibit a notably heightened level of heat and mass transfer. Furthermore, these regions display a more pronounced temperature profile, while the quantity of liquid within the tank is comparatively greater. Additionally, the pressure distribution within the tank is more intense, particularly in areas where the liquid content is higher.
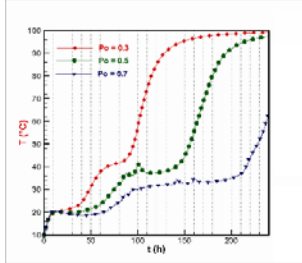
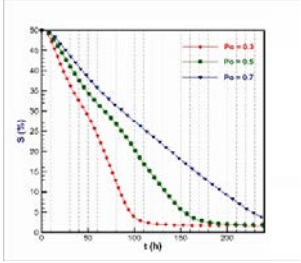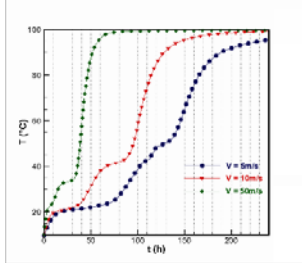We have also studied the effects of the following parameters:
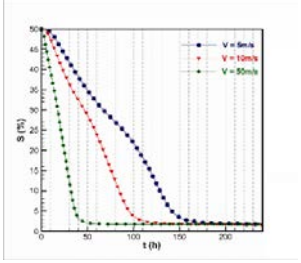
- Liquid saturation: $S = 20\% - 50\% - 80\%$.
- Porosity: $Po = 0.3 - 0.5 - 0.7$.
- Air velocity: $5 - 10 - 50$ m/s.

The following table presents these effects (**Table 3**):

Table 3. Parameters effects.

Effect	Temperature comparison	Saturation comparison
Saturation		

Table 3. (*Continued*).

Effect	Temperature comparison	Saturation comparison
Porosity		
Velocity		

Based on these observations, the following effects can be noted:

● A reduction in liquid saturation ($S = 20\%$) leads to a more intense and rapid heat and mass transfer within the ceramic tank.

● An increase in porosity rate ($Po = 0.7$) results in a less pronounced distribution of temperature and saturation over time.

● Enhanced heat transfer rate ($V = 50$ m/s) accelerates and intensifies the evolutions of temperature and saturation within the tank.

Our model provides an estimation of thermal transport within a ceramic tank featuring five cavities. These cavities are heated to 100 °C, with a hot air velocity of 10 m/s, aiming to heat the tank and investigate the heat and mass transfer phenomena occurring between the ceramic grains. The results reveal distinct thermal evolutions between the exchange surface and the grains within the reservoir: the grains at the exchange surface displaying the most rapid evolutions. This observation is supported by the cross-sectional views. Furthermore, an analysis of the effects of temperature, saturation, and velocity is presented, yielding the following findings:

● The decreasing saturation leads to faster distribution of temperature and saturation.
● The increased porosity between the grains results in more intense and rapid thermal evolution.
● The reducing the velocity leads to a slower process.

6. Conclusion

In this study, a three-dimensional code is presented to investigate the interconnected mass and heat transport processes taking place within a ceramic tank. The implementation of this numerical code serves to enhance our understanding of the phenomena inherent in porous transport. The mesh generation is accomplished using the Gmsh, and a dedicated model is devised for the 3D thermal transfer in the porous ceramic tank.

We conduct a thermal investigation on a porous ceramic tank, focusing on the study of its thermal transport characteristics in relation to the surrounding environment. This analysis encompasses the examination of heat and mass distribution within the tank. Additionally, we assess the impact of three key

11

parameters—saturation, porosity, and air velocity—on the tank's thermal performance. The obtained results present an important analysis for the determining of suitability of the ceramic tank for its intended purpose, as well as facilitating the design of an efficient insulation system to mitigate heat loss or gain.

Author contributions

Conceptualization, RR and NBK; methodology, RR; software, NBK; validation, NBK; formal analysis, MM; investigation, RR; resources, RR; data curation, RR; writing—original draft preparation, RR; writing—review and editing, RR; visualization, RR; supervision, RR; project administration, RR; funding acquisition, NBK. All authors have read and agreed to the published version of the manuscript.

Acknowledgments

Conflict of interest

The authors declare no conflict of interest.

Nomenclature

C_a: air's specific heat kJ/kg. K

C_p: specific heat with constant pressure kJ/k. gK

C_v: vapor phase's specific heat kJ/kg. K

C_w: water's specific heat kJ/kg. K

$D_{A,B}$: diffusion's coefficient m^2/s

g: acceleration due to gravity m/s^2

h_{mt}: mass transfer coefficient m/s

h_{ht}: heat transfer coefficient W/m^2. ℃

K: permeability m^2

L: tank's characteristic length m

M_a: air's molecular mass kg/mol

M_v: vapor phase's molecular mass kg/mol

$\dot{m}$: evaporation rate kg/s

n_i: outwardly oriented normal vector

P: pressure Pa

Pc: capillary pressure Pa

Po: tank porosity %

P_{Vs}: saturated vapor phase pressure Pa

R: gas's constant kJ/k. mol. K

r: the characteristic value representing the average curvature radius of the menisci is determined when the liquid retention forces are attributed to capillary forces

S: saturation of liquid %

T: process temperature K

t: time s

v_a: air's velocity m/s

Dimensionless numbers

Re: Reynolds symbol

Pr: Prandtl symbol

Sc: Schmidt symbol

Symbols

ε: medium's porosity

ε_l: liquid's fraction

μ: dynamical viscosity kg/m. s

ϑ: kinematical viscosity m^2/s

ρ: medium density kg/m^3

λ: coefficient of conductive transfer W/m. ℃

σ: tension of surface N/m

ΔH_{vap}: latent heat of vaporization J/kg

Subscripts

0: state initial

a: phase of air

eff: effective term

g: phase of gas

l: phase of liquid

v: phase of vapor

vs: saturated vapor

References

1. Luikov AV. Systems of differential equations of heat and mass transfer in capillary porous bodies. *International Journal of Heat and Mass Transfer* 1975; 18(1): 1–14. doi: 10.1016/0017-9310(75)90002-2
2. Whitaker S. *Simulation Heat, Mass and Momentum Transfer in Porous Media: A Theory of Drying*. Academic Press; 1977.
3. Kabeel AE, Abdelgaied M. Numerical and experimental investigation of a novel configuration of indirect evaporative cooler with internal baffles. *Energy Conversion and Management* 2016; 126: 526–536. doi: 10.1016/j.enconman.2016.08.028

4. Hettiarachchi HDM, Golubovic M, Worek WM. The effect of longitudinal heat conduction in cross flow indirect evaporative air coolers. *Applied Thermal Engineering* 2007; 27(11–12): 1841–1848. doi: 10.1016/j.applthermaleng.2007.01.014

5. Fung LSK, Hiebert AD, Nghiem LX. Reservoir simulation with a control volume finite element method. *SPE Reservoir Engineering* 1992; 7(3): 349–357. doi: 10.2118/21224-PA

6. Abdelsalam SI, Alsharif AM, Abd Elmaboud Y, Abdellateef AI. Assorted kerosene-based nanofluid across a dual-zone vertical annulus with electroosmosis. *Heliyon* 2023; 9(5): e15916. doi: 10.1016/j.heliyon.2023.e15916

7. Li J, Rajajayavel SRC, Ghoshal S. Transport of carboxymethyl cellulose-coated zerovalent iron nanoparticles in a sand tank: Effects of sand grain size, nanoparticle concentration and injection velocity. *Chemosphere* 2016; 150: 8–16. doi: 10.1016/j.chemosphere.2015.12.075

8. Kiwan S, Soud QR. Experimental investigation of the thermal performance of a sand-basalt heat storage system for beam-down solar concentrators. *Case Studies in Thermal Engineering* 2020; 19: 100609. doi: 10.1016/j.csite.2020.100609

9. Cao Y, Ayed H, Algelany AM, et al. Receiving heat from a PCM tank by using natural convection of water and NEPCM: A simulation for LHTES application. *Case Studies in Thermal Engineering* 2022; 35: 102123. doi: 10.1016/j.csite.2022.102123

10. Al-Yaqoubi S, Al-Maktoumi A, Kacimov A, et al. Fresh-saline water dynamics in coastal aquifers: Sand tank experiments with MAR-wells injecting at intermittent regimes. *Journal of Hydrology* 2021; 601: 126826. doi: 10.1016/j.jhydrol.2021.126826

11. Thien FY, Hamasaki K, Shapawi R, et al. Effect of background tank color in combination with sand substrate and shelters on survival and growth of Scylla tranquebarica instar. *The Egyptian Journal of Aquatic Research* 2022; 48(3): 241–246. doi: 10.1016/j.ejar.2022.04.004

12. Zuo Y, Zhang M, Cheng F, Zhou H. Experimental investigation of the migration and solidification characteristics of Solar Salt in hot sand layer of tank foundation. *Applied Thermal Engineering* 2023; 219, Part B: 119571. doi: 10.1016/j.applthermaleng.2022.119571

13. Lee JH, Lee SH, Han SW. Nonlinear earthquake responses of unanchored cylindrical liquid storage tanks on flexible soil. *Structures* 2023; 54: 1465–1490. doi: 10.1016/j.istruc.2023.05.070

14. Moreno M, Colombo J, Wilches J, et al. Buckling of steel tanks under earthquake loading: Code provisions vs FEM comparison. *Journal of Constructional Steel Research* 2023; 209: 108042. doi: 10.1016/j.jcsr.2023.108042

15. Abdellatif HE, Belaadi A, Alshahrani H, et al. Modeling three-dimensional flow in a thermal energy tank: Numerical analysis of the impact of tank shape on the melting and solidification of phase change material. *Journal of Energy Storage* 2023; 72, Part A: 108286. doi: 10.1016/j.est.2023.108286

16. Dittus FW, Boelter LMK. Heat transfer in automobile radiators of the tubular type. *International Communications in Heat and Mass Transfer* 1985; 12(1): 3–22. doi: 10.1016/0735-1933(85)90003-X

17. Balliga BR, Patankar SV. A new finite-element formulation for convection-diffusion problems. *Numer Heat Transfer* 2007; 3: 393–409. doi: 10.1080/01495728008961767

18. Balliga BR, Patankar SV. A contro volume finite-element method for two-dimensional fluid flow and heat transfer. *Numerical Heat Transfer* 2007; 6: 245–261. doi: 10.1080/01495728308963086

19. Geuzaine C, Remacle JF. Gmsh: A 3-D finite element mesh generator with built-in pre- and post-processing facilities. *International Journal for Numerical Methods in Engineering* 2009; 79 (11): 1309–1331. doi: 10.1002/nme.2579

Appendix

<div align="center">

Table A1. The characteristics of air.

</div>

Properties of the material	Input values
Specific heat capacity	1.006×10^3 J/kg. K
Thermal conductance	2.6×10^{-2} W/m. K
Air density	0.117×10^1 kg/m³
Dynamical viscosity	0.115×10^{-6} kg/m. s

<div align="center">

Table A2. The characteristics of ceramic tank.

</div>

Properties of the material	Input values
Ceramic porosity	3.6×10^{-1}
Phase solid's density	$\rho_s = 2600$ kg/m³
Solid's specific heat capacity	$C_{ps} = 879$ J/kg. K
Liquid's specific heat capacity	$C_{pl} = 4220$ J/kg. K
Vapor's specific heat capacity	$C_{pv} = 0.186 \times 10^4$ J/kg. K
Liquid's dynamical viscosity	$\mu_l = 65 \times 10^{-5}$ kg/m. s
Vapor's dynamical viscosity	$\mu_v = 186 \times 10^{-7}$ kg/m. s
Liquid's intrinsically permeability	0.25×10^{-13} m²
Liquid's relative permeability	$K_l = X^3; X = \frac{X - X_{ir}}{X_{sat} - X_{ir}}$ with $X_{ir} = 0.3$
Gas's relative permeability	$K_{rg} = (2X - 3)X^2 + 1$
Capillary pressure	$P_c = \left(\frac{\varepsilon}{K}\right)^{\frac{1}{2}} \sigma J(s)$ with $$J(s) = 364 \times 10^{-3}[1 - exp(40s - 40)] + 221 \times 10^{-3}(1 - s) + \frac{0.005}{s - 0.05}$$ and $\sigma(T) = (0.1212 - 0.167 \times 10^{-3}T$
Pressure (vapor)	$< P_v >=< P_{vs} > exp[-\frac{2\sigma M_v}{r\rho_l R < T >}]$ with $\log_{10}(r) = 2.16 \times 10^{-2} + 43.85 - 253.5 \times S^2 + 794.54 \times S^3 - 1333.7 \times S^4 + 1111 \times S^5 - 352.5 \times S^6$
Thermal conductivity	$\lambda_{eff} = (\lambda_g^a(\varepsilon - \varepsilon_l) + \lambda_l^a \varepsilon_l + \lambda_s^a(1 - \varepsilon))^{1/a}$ W/m. K with $a = 0.25$